







# Combined Neutron and X-Ray Tomography—A Versatile and Non-Destructive Tool in Planetary Geosciences



### Key Points:

- Combined neutron and X-ray imaging was used to locate projectile material and hydrous phases in meteorites and terrestrial impactites
- Locating and identifying projectile material can shed light on the impact cratering process
- Combined neutron/X-ray tomography can serve as a fundamental method for the characterization of material from (future) sample return missions

**J. Martell**<sup>1,2</sup> , **C. Alwmark**<sup>1</sup> , **R. Woracek**<sup>3</sup>, **S. Alwmark**<sup>1,4</sup> , **S. Hall**<sup>2,5</sup>, **L. Ferrière**<sup>6</sup> , **L. Daly**<sup>7,8,9</sup>, **C. Bender Koch**<sup>10</sup> , **J. Hektor**<sup>11</sup> , **S. Johansson**<sup>5</sup>, **L. Helfen**<sup>12</sup>, **A. Tengattini**<sup>12</sup>, and **D. Mannes**<sup>13</sup>

<sup>1</sup>Department of Geology, Lund University, Lund, Sweden, <sup>2</sup>LINXS Institute of Advanced Neutron and X-ray Science, Lund, Sweden, <sup>3</sup>European Spallation Source, Lund, Sweden, <sup>4</sup>Niels Bohr Institute, University of Copenhagen, Copenhagen, Denmark, <sup>5</sup>Department of Solid Mechanics, Lund University, Lund, Sweden, <sup>6</sup>Natural History Museum Vienna, Vienna, Austria, <sup>7</sup>School of Geographical and Earth Sciences, University of Glasgow, Glasgow, UK, <sup>8</sup>Australian Centre for Microscopy and Microanalysis, The University of Sydney, Sydney, NSW, Australia, <sup>9</sup>Department of Materials, University of Oxford, Oxford, UK, <sup>10</sup>Department of Chemistry, University of Copenhagen, Universitetsparken 5, Copenhagen, Denmark, <sup>11</sup>Department of Materials Science and Applied Mathematics, Malmö University, Malmö, Sweden, <sup>12</sup>Institut Laue Langevin, Grenoble, France, <sup>13</sup>Paul Scherrer Institut, Villigen, Switzerland

### Supporting Information:

Supporting Information may be found in the online version of this article.

### Correspondence to:

C. Alwmark,  
[carl.alwmark@geol.lu.se](mailto:carl.alwmark@geol.lu.se)

### Citation:

Martell, J., Alwmark, C., Woracek, R., Alwmark, S., Hall, S., Ferrière, L., et al. (2024). Combined neutron and x-ray tomography—A versatile and non-destructive tool in planetary geosciences. *Journal of Geophysical Research: Planets*, 129, e2023JE008222. <https://doi.org/10.1029/2023JE008222>

Received 17 NOV 2023  
Accepted 26 JAN 2024

**Abstract** With several upcoming sample return missions, such as the Mars Sample Return Campaign, non-destructive methods will be key to maximizing their scientific output. In this study, we demonstrate that the combination of neutron and X-ray tomography provides an important tool for the characterization of such valuable samples. These methods allow quantitative analyses of internal sample features and also provide a guide for further destructive analyses with little to no sample treatment, which maintains sample integrity, including minimizing the risk of potential contamination. Here, we present and review the results from four case studies of terrestrial impactites and meteorites along with their analytical setup. Using combined X-ray and neutron tomography, a Ni-Fe silicide spherule, that is, projectile material, was located within a Libyan Desert Glass sample and the distribution of hydrous phases was pinpointed in selected impactite samples from the Chicxulub IODP-ICDP Expedition 364 drill core and the Luizi impact structure, as well as in the Miller Range 03346 Martian meteorite.

**Plain Language Summary** Neutron and X-ray tomography give complementary three-dimensional information about the distribution of different phases within a geologic sample. We demonstrate that these two methods can be successfully used to locate meteoritic material (i.e., from the impacting object) and hydrous components in terrestrial impactites and meteorites. This can help shed light on aqueous processes in the Solar System as well as the impact cratering process. Non-destructive methods like these will be important for upcoming sample return missions to characterize the returned samples and guide further destructive analyses.

## 1. Introduction

The exploration of the rocky bodies in our Solar System is traditionally achieved using remote sensing data, studying terrestrial analog sites, and analyses of physical samples (including meteorites, samples from impact structures on Earth, and from return sample missions) and also from in situ measurements using rovers (e.g., on Mars; Farley et al., 2022; Liu et al., 2022; Murchie et al., 2007; Toulmin et al., 1977). Physical samples from other celestial bodies than the Earth are limited to meteorites and material from sample return missions, for example, lunar samples from the Apollo and Luna programs as well as from the recent Chang'e 5 mission, Stardust from comet 81P/Wild 2, and asteroid regolith samples from Bennu by the OSIRIS-Rex mission, and from Itokawa and Ryugu using the Hayabusa and Hayabusa2 missions, respectively (e.g., Brownlee et al., 2006; Kawaguchi et al., 2008; Lauretta et al., 2017). Major unanswered scientific questions motivate(d) the return of these materials for the study on Earth, such as the potential to shed light on the delivery of water and organic molecules to the early Earth, the origin of life, the confirmation of potential past presence of life forms on other celestial bodies than Earth, the origin of the Moon, comet compositions, mixing and distribution of materials in the solar nebula, and details regarding planetary accretion (e.g., Beaty et al., 2019; Brownlee et al., 2006; Che et al., 2021; Lock et al., 2020; Yada et al., 2022).

A large number of available analytical methods used to characterize and understand these samples are destructive by nature, for example, detailed chemical and isotope analyses are usually performed by crushing or dissolving

the sample, and petrological characterization is made on polished (thin) sections. These methods are also, in a way, “blind”—in that there is no way of knowing what is inside a sample before cutting it open, which means that there is always a risk that potentially interesting regions or phases are lost or overlooked during cutting or while using other sample preparation methods. One way to circumvent these issues is to utilize non-destructive tomographic methods, with the most commonly used method being X-ray computed tomography (XCT; e.g., Hanna & Ketcham, 2017, and references therein). XCT is a relatively easily accessible technique, as it can be performed both with laboratory-based machines, which are now available in many research institutions worldwide, and at synchrotron sources for imaging with higher spatial resolution (Cnudde & Boone, 2013; Hanna & Ketcham, 2017; Hezel, Elangovan, et al., 2013). Over the last two decades, XCT of planetary materials has contributed to major advances in planetary science, providing insight into the 3D mineralogy and deformation textures of meteorites (e.g., Alwmark et al., 2011; Hanna et al., 2022; Hezel, Friedrich, & Uesugi, 2013; Kadlag et al., 2023; Krzesińska, 2011; Lemelle et al., 2004; Soini et al., 2023), asteroid particles from Hayabusa (Tsuchiyama et al., 2013), lunar soil samples (the Apollo Next Generation Sample Analysis; Gross et al., 2023) and some terrestrial impactites, such as impact breccias from the Bosumtwi, the Kara, and the Ries impact structures, and also a Muong Nong-type tektite (Koeberl et al., 2002; Zubov et al., 2021).

A complementary 3D imaging method to XCT is neutron computed tomography (NCT). In contrast to XCT, NCT is a less commonly used method, in part because it requires large-scale neutron facilities only available in a limited number of locations worldwide. Nevertheless, NCT has been used for non-destructive structural characterization of iron meteorites (Caporali et al., 2016; Peetermans et al., 2013) and chondrite meteorites (Kichanov et al., 2022). In addition, a few studies have used combined NCT and XCT to study various types of impactites and meteorites; these studies have provided insight into the distribution of hydrogen in Martian meteorites (Martell et al., 2022) and chondrite meteorites (Treiman et al., 2018, 2022), as well as petrographic characterization of terrestrial impactites (Fedrigo et al., 2018; Needham et al., 2020; Pakhnevich, 2016; Steen Duchnik et al., 2012).

Here, we present the results from four case studies of geological (planetary) samples: (a) a sample of Libyan Desert Glass (LDG); (b) a claystone sample from the Chicxulub IODP-ICDP Expedition 364 drill-core; (c) a sample of impact melt rock from the Luizi impact structure; and (d) a sample of the Martian nakhlite meteorite Miller Range (MIL) 03346. We were interested in these samples because we wanted to locate and describe the carrier phase for extraterrestrial geochemical signature in impactites, and because we wanted to understand propagation paths and dynamics of fluids in impactites and extraterrestrial samples (see details below). We demonstrate how combined NCT and XCT methods can be used to locate remnant projectile material and map hydrous phases in various geological samples. Furthermore, we describe how the tomography data can be used to guide complementary investigations, for example, using light microscopy and scanning electron microscopy (SEM).

### 1.1. Traces of Impactor Projectiles

Currently, there are ~200 confirmed impact structures on Earth (Osinski et al., 2022), but the type of projectile is known only for a handful number of them (see e.g., Koeberl et al., 2007; Tagle & Claeys, 2005). Physical impactor fragments are very rarely recovered within hypervelocity impact structures since enormous pressures and temperatures result in almost complete vaporization of the impactor (French, 1998). Nevertheless, a projectile component can be recognized within impactites by enhanced abundances of certain siderophile elements (such as Ni, Cr, Co), particularly the platinum group elements (PGEs) (Ru, Rh, Pd, Os, Ir, Pt; Koeberl, 1998), and their characteristic meteoritic isotope ratios (e.g., Re-Os isotope ratios; Koeberl & Shirey, 1997), such as within impact melt rocks and more rarely within suevitic (melt-bearing) impact breccias (Koeberl, 1998). The best example of such a projectile component is the Ir enrichment (several thousand times higher than the average upper continental crust) observed at the K–Pg boundary layer, found at more than 120 locations worldwide (Alvarez et al., 1980; Koeberl et al., 2012; Schulte et al., 2010). However, the fate of the projectile during the impact process is still not completely understood, for example, processes taking place inside the impact vapor cloud, and what the possible PGE carrier phases such as metallic alloys look like and how they form (Goderis et al., 2013). Meteoritic material is generally heterogeneously distributed within impactites (Feignon et al., 2022), likely in the form of micrometer-sized PGE nuggets (Goderis et al., 2012; Mohr-Westheide et al., 2018) or even finer particles. Thus, combining NCT and XCT and focusing on locating PGE nuggets within impactites could enable detailed investigation of projectile material within impactites, and consequently circumvent issues with whole-rock techniques that require

a significant amount of material. In the LDG and the Chicxulub drill core samples presented herein, combined NCT and XCT aim at pinpointing the projectile material in these impactites.

## 1.2. Aqueous Processes and Impact Cratering

Impact events can induce large-scale hydrothermal systems, where hot fluids circulate through the bedrock for thousands to millions of years (e.g., Kring et al., 2020). These environments might have been favorable for the origin of life on Earth and possibly on other planets such as Mars, if life ever existed there (e.g., Farmer, 2000; Osinski et al., 2013). Olivine grains in the nakhlite group of Martian meteorites are often cross-cut by pre-terrestrial clay minerals, which confirm that Mars once had liquid water (Day et al., 2006; Treiman, 2005; Udry et al., 2012). The correlation between shock deformation features in mineral grains and secondary aqueous alteration phases within Martian meteorites suggests that impact event(s) facilitated the water-rock interaction needed to alter the minerals (Daly et al., 2019; Martell et al., 2022). Confirming the presence of hydrous phases in a sample is usually performed indirectly by identifying hydrogen-bearing minerals using for example, petrographic or/and electron microscopy, following destructive sample handling. In this study, the MIL 03346,231 meteorite and Luizi impact melt rock samples were imaged with XCT and NCT to investigate hydrous phases and their 3D distribution with a non-destructive approach.

## 1.3. Principles of NCT/XCT

The interactions between neutrons and matter are relatively weak compared to that of X-rays. In XCT, the incoming photons (X-rays) interact with the electrons in the sample material, whereas neutrons interact with the atomic nuclei, in both cases leading to attenuation due to scattering or absorption. The different interaction mechanisms lead to different attenuation by the same materials, such that attenuation due to neutrons may be weaker or stronger than for X-rays, giving different contrasts in tomographic images. The information from NCT and XCT is therefore often highly complementary. Even in the case of heavy elements, the interaction with neutrons can be relatively weak compared to X-rays, which allow neutrons to penetrate (some) heavy matter more easily. Additionally, neutrons interact differently with different isotopes of a given element (e.g.,  $^{235}\text{U}/^{238}\text{U}$  and  $^1\text{H}/^2\text{H}$ ; Sears, 1992; Strobl et al., 2009). The difference in neutron/X-ray attenuation for all the elements is visualized in the two shaded periodic tables (Figure 1). Since X-rays interact with the electron in the cloud of an atom, the X-ray attenuation increases with the atomic number (i.e., the number of electrons). In contrast, as neutrons interact with the nucleus of the atom, neutron attenuation is not dependent on the atomic number, leading to a seemingly irregular pattern (Lehmann & Kardjilov, 2008). Neutrons are particularly “sensitive” to certain PGEs such as iridium (Tengattini et al., 2021) and, unlike X-rays, also to hydrogen and chlorine (Kardjilov et al., 2018). These elements are highly relevant within the field of planetary geology; iridium can be used to detect and confirm a meteoritic component within impactites (e.g., Koeberl et al., 2012), and the distribution of hydrogen in meteorites can shed light on aqueous processes on Solar System bodies and their driving forces in the early Solar System (e.g., Treiman et al., 2022). Furthermore, deciphering fluid pathways within meteorites can give insight into the source and timing of the fluids, as well as the degree of terrestrial weathering of recovered meteorites (Martell et al., 2022).

The setups for NCT and XCT are based on the same principle: a sample is placed on a rotation stage between a detector and a source, and radiographic projections are collected while the sample is rotated, usually over  $180^\circ$ – $360^\circ$ . The detector measures the decrease in intensity, compared to the incident beam, after it has passed through and interacted with the sample, that is, the attenuation. The degree of attenuation is dependent on the interaction between neutrons or X-ray photons and the sample material as well as the amount of material traversed. The relationship between the initial intensity of the source and the final intensity at the detector is generally described by Lambert-Beer's Law. Assuming a homogenous sample, this law states that:

$$I = I_0 e^{-\mu x}$$

The equation describes the transmitted intensity,  $I$ , of an incoming monochromatic beam with a certain photon intensity  $I_0$  that penetrates a sample with a thickness  $x$  and with an attenuation coefficient  $\mu$  (e.g., in  $\text{cm}^{-1}$ ). For non-homogenous materials, the attenuation coefficient is a function of the position and depends on the material at each position. The distance,  $x$ , describes the path length through the material; thus, the equation is usually written

Attenuation coefficients for thermal neutrons (cm<sup>-1</sup>)

1a	2a	3b	4b	5b	6b	7b	8				1b	2b	3a	4a	5a	5a	7a	0
H																	He	
3.44																	0.02	
Li	Be											B	C	N	O	F	Ne	
3.30	0.79											101.60	0.56	0.43	0.17	0.20	0.10	
Na	Mg											Al	Si	P	S	Cl	Ar	
0.09	0.15											0.10	0.11	0.12	0.06	1.33	0.03	
K	Ca	Sc	Ti	V	Cr	Mn	Fe	Co	Ni	Cu	Zn	Ga	Ge	As	Se	Br	Kr	
0.06	0.08	2.00	0.60	0.72	0.54	1.21	1.19	3.92	2.05	1.07	0.35	0.49	0.47	0.67	0.73	0.24	0.61	
Rb	Sr	Y	Zr	Nb	Mo	Tc	Ru	Rh	Pd	Ag	Cd	In	Sn	Sb	Te	I	Xe	
0.08	0.14	0.27	0.29	0.40	0.52	1.76	0.58	10.88	0.78	4.04	115.11	7.58	0.21	0.30	0.25	0.23	0.43	
Cs	Ba	La	Hf	Ta	W	Re	Os	Ir	Pt	Au	Hg	Tl	Pb	Bi	Po	At	Rn	
0.29	0.07	0.52	4.99	1.49	1.47	6.85	2.24	30.46	1.46	6.23	16.21	0.47	0.38	0.27				
Fr	Ra	Ac	Rf	Ha														
	0.34																	
	Ce	Pr	Nd	Pm	Sm	Eu	Gd	Tb	Dy	Ho	Er	Tm	Yb	Lu				
*Lanthanides	0.14	0.41	1.87	5.72	171.47	94.58	1479.04	0.93	32.42	2.25	5.48	3.53	1.40	2.75				
**Actinides	Th	Pa	U	Np	Pu	Am	Cm	Bk	Cf	Es	Fm	Md	No	Lr				
	0.59	8.46	0.82	9.80	50.20	2.86												

Attenuation coefficients for thermal X-rays (cm<sup>-1</sup>) (150 kV)

1a	2a	3b	4b	5b	6b	7b	8				1b	2b	3a	4a	5a	6a	7a	0
H																	He	
0.02																	0.02	
Li	Be											B	C	N	O	F	Ne	
0.06	0.22											0.28	0.27	0.11	0.16	0.14	0.17	
Na	Mg											Al	Si	P	S	Cl	Ar	
0.13	0.24											0.38	0.33	0.25	0.30	0.23	0.20	
K	Ca	Sc	Ti	V	Cr	Mn	Fe	Co	Ni	Cu	Zn	Ga	Ge	As	Se	Br	Kr	
0.14	0.26	0.48	0.73	1.04	1.29	1.32	1.57	1.78	1.96	1.97	1.64	1.42	1.33	1.50	1.23	0.90	0.73	
Rb	Sr	Y	Zr	Nb	Mo	Tc	Ru	Rh	Pd	Ag	Cd	In	Sn	Sb	Te	I	Xe	
0.47	0.86	1.61	2.47	3.43	4.29	5.06	5.71	6.08	6.13	5.67	4.84	4.31	3.98	4.28	4.06	3.45	2.53	
Cs	Ba	La	Hf	Ta	W	Re	Os	Ir	Pt	Au	Hg	Tl	Pb	Bi	Po	At	Rn	
1.42	2.73	5.04	19.70	25.47	30.49	34.47	37.92	39.01	38.61	35.94	25.88	23.23	22.81	20.28	20.22		9.77	
Fr	Ra	Ac	Rf	Ha														
	11.80	24.47																
	Ce	Pr	Nd	Pm	Sm	Eu	Gd	Tb	Dy	Ho	Er	Tm	Yb	Lu				
*Lanthanides	5.79	6.23	6.46	7.33	7.68	5.66	8.69	9.46	10.17	10.91	11.70	12.49	9.32	14.07				
**Actinides	Th	Pa	U	Np	Pu	Am	Cm	Bk	Vf	Es	Fm	Md	No	Lr				
	28.95	39.65	49.08															

**Figure 1.** Neutron and X-ray interactions with matter, darker colors represent higher attenuation. Neutrons interact with the nucleus in the atom cloud, and the attenuation is thus not dependent on the number of electrons in an element. On the contrary, X-rays interact with the electrons of the atom, and the attenuation coefficient thus increases with the atomic number. Hydrogen and iridium are marked with red boxes; hydrogen is only highly attenuated for neutrons, while iridium is highly attenuated for both X-rays and neutrons. Figure is adapted from Lehmann et al. (2022).

as an integral over the full path length through the sample. For a non-monochromatic incident radiation, the attenuation coefficient is a function of the energy.

Reconstruction algorithms such as filtered backprojection transform the projections into a set of 2D slices that, when “stacked” into a 3D volume, contain the attenuation in each voxel (a 3D pixel) represented by a grayscale value. This stack can be rendered as a 3D volume for the visualization of the 3D structure. As geological samples are often heterogenous in nature, including below the voxel scale, the grayscales in the reconstructed tomography images represent an average of the elements within each specific voxel region.

The spatial resolution in tomography is a function of both the detector characteristics, the beam divergence, and the reconstruction algorithms used. Compared to XCT, NCT yields a comparably low resolution (usually tens of micrometers), while synchrotron sources can give resolutions down to the nanometer level for small samples.



**Table 1**  
*Analytical Details for X-Ray and Neutron Tomography*

Imaging setup					
	Sample	Luizi	Libyan Desert Glass	MIL 03346,231	Chicxulub core sample
	Neutron facility (beamline)	ILL (NeXT)	PSI (ICON)	ILL (NeXT)	ILL (NeXT)
	X-ray facility	LTH 4D imaging lab	LTH 4D imaging lab	LTH 4D imaging lab	LTH 4D imaging lab
Neutrons	Rotating angle (°)	360	360	360	360
	Voxel size (μm)	15.9	31.7	7.15	7.15
X-rays	Rotating angle (°)	360	360	360	360
	Voxel size (μm)	9	45	5.75	17
	Source voltage (kV)	80	80	60	80

Note. PSI: Paul Scherrer Institut, ILL: Institut Laue-Langevin.

However, NCT has the advantage of being able to probe larger samples, and the spatial resolution is constantly improving. The most powerful neutron sources today can offer a resolution below  $\sim 4$  μm depending on sample size and sample properties (Tengattini et al., 2022). Also, some facilities host systems that allow simultaneous neutron and X-ray tomograms, such as the U.S. National Institute of Standards and Technology (LaManna et al., 2017). Even better results are expected from next-generation neutron sources such as the European Spallation Source (ESS) in Sweden (Andersen et al., 2020). The neutron energy spectrum also plays a role; samples can be imaged using either cold or thermal neutrons (where the former have lower energy and longer wavelengths and the latter has higher energy and, thus shorter wavelengths). The use of cold neutrons increases the probability of interaction with the nuclei, yielding better image contrast and, therefore, enabling resolution of finer structures. Cold neutrons are thus a good choice for small and weakly attenuating samples (Lehmann & Kardjilov, 2008).

## 2. Experimental Setup and Case Studies

All four samples were measured using neutron tomography: the LDG sample at the ICON beamline at the Paul Scherrer Institut (PSI) in Switzerland (beamline specifics in Kaestner et al., 2011), and the other three samples (MIL 03346,231, Chicxulub drill core sample, and Luizi impact melt rock sample) at the NeXT imaging beamline at Institut Laue Langevin (ILL) in France (beamline specifics in Tengattini et al., 2020). Both beamlines use a neutron spectrum with a broad wavelength distribution, while the exact wavelength spectra differ between the beamlines. High-resolution X-ray tomography was performed on all four samples at the 4D Imaging Lab at Lund University in Sweden. For all the tomography experiments, samples were scanned without any prior preparation or treatment and simply placed on sample holders. The different resolutions of the samples in this study were a compromise between for example, allocated beam time and sample size (and thus the Field of view or “FoV”) and an acceptable signal-to-noise ratio, for example, depending on the contrast between different features in the sample. Analytical details for the X-ray and neutron tomographic acquisition for each case study are given in Table 1.

Scanning electron microscopy images were acquired at the Department of Geology at Lund University in Sweden, using a Tescan Mira3 High-Resolution Schottky field-emission SEM equipped with an Oxford Energy-Dispersive X-ray Spectroscopy system (EDS; X-MaxN 80, 124 eV, 80 mm<sup>2</sup>). The SEM was operating at 15 kV, in high vacuum and at a working distance of 15 mm. Before the SEM imaging, all samples but MIL 03346,231 were manually cut and polished to expose the interior of regions-of-interest. The SEM-EDS analyses could then be used to validate the phase segmentation. Depending on the sample (e.g., hardness, shape), some samples were cast in epoxy for convenience, before being coated with a 15 nm layer of carbon to avoid charging effects.

Following the tomography, images were reconstructed into a stack of slices using the Tofu software (Fragó et al., 2022), and the resulting 3D images were registered (i.e., aligned) using the software spam (Software for Practical Analysis of Materials) and multi-modal registration (Stamati et al., 2020). Segmentation and renderings were performed using ImageJ (Schindelin et al., 2012) and Dragonfly (Dragonfly 2021.1 [Computer software], 2021).

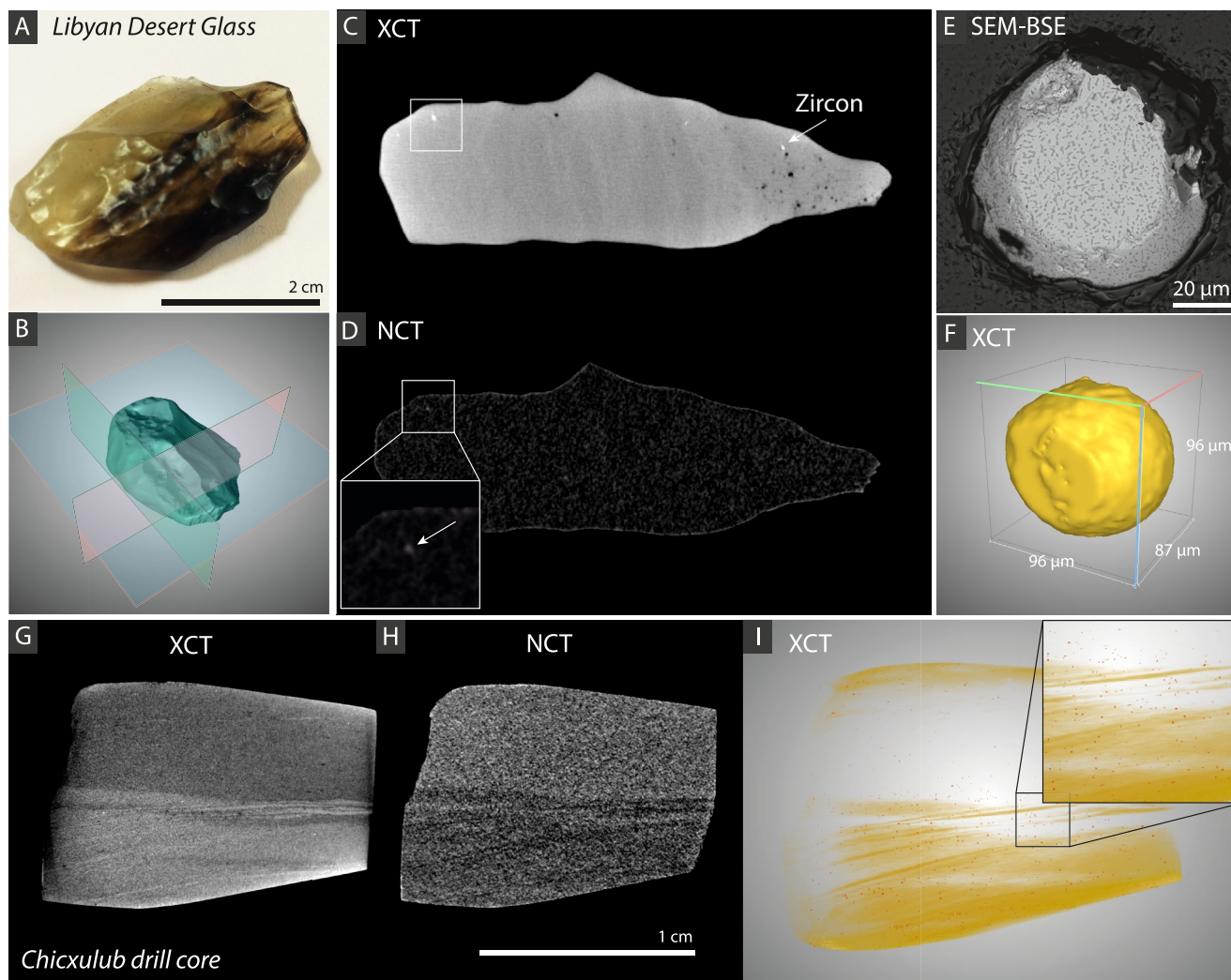


**Figure 2.** (a) Libyan desert glass (LDG) sample, note the distinct and parallel dark bands. (b) 3D rendering of the LDG sample, with planes for x, y, and z views intersecting at the FeNi-spherule. These were used as a guide when polishing the sample. (c) X-ray slice. The white box marks highly attenuating inclusion visible with both neutron computed tomography (NCT) and XCT. A faint banding can be seen as well as a zircon grain, which is only visible in the XCT image. (d) Corresponding neutron slice, with the white box showing a zoomed in view of the inclusion. (e) BSE image of the polished sample with the inclusion exposed (FeNi silicide spherule). (f) High-resolution (0.5  $\mu\text{m}$ ) 3D image of the inclusion. The flat surface corresponds to the surface in panel (e). (g) X-ray slice of the Chicxulub drill core sample. Note a banding in the lower half of the sample, corresponding to compositional differences in Si, Mg and Al. (h) corresponding neutron slice. The banding is visible, but bright bands in the XCT images have low attenuation in the NCT images, and vice versa. (i) 3D rendering of the Chicxulub sample based on the XCT images, showing the bright banding in yellow. The red specks in the close-up are pyrite grains, which are mainly located in the bright bands.

## 2.1. Libyan Desert Glass (LDG)

LDG is a  $\sim 28.5$  Ma old (Bigazzi & De Michele, 1996), silica-rich impact glass ( $\sim 98$  wt.%  $\text{SiO}_2$ ) found as cm to dm-sized pieces in the southwestern corner of the Great Sand Sea in western Egypt, near the Libyan border (see e. g., Cavosie & Koeberl, 2019; Cipriani et al., 2000; Giuli et al., 2003; Koeberl, 2000, and references therein). The sample analyzed in this study is an approximately 3-1.0.5 cm-sized piece of glass (Figure 2a). The color ranges from a yellow-tinted transparent part to an LDG-characteristic brown banding (Figure 2a).

### 2.1.1. Results

Figure 2b shows a 3D rendering of the registered XCT and NCT volumes, with orthogonal planes (for x, y, and z) added, from which a slice-by-slice comparison can be made. Tiny nm-to- $\mu\text{m}$ -sized vesicles are visible in both the XCT and NCT data sets and are mainly located in the transparent and “frothy” areas, in agreement with earlier studies (Aboud, 2009). Parallel banding is only faintly visible in the XCT images (Figure 2c). Several bright,

highly attenuating inclusions are present in the XCT data set and SEM analysis of polished sections shows that these generally correspond to zircon grains. Zircon ( $ZrSiO_4$ ) has a low neutron attenuation and grains are thus not resolvable in the NCT images. Interestingly, the slice-by-slice comparison revealed one,  $\sim 80$   $\mu m$  sized, spherical inclusion with high attenuation in both modalities (Figures 2c and 2d; Figures S1 and S2 in Supporting Information S1). After locating the inclusion within the rendering, the planes were set so they would intersect exactly at the location of the inclusions (Figure 2b) and the sample was then manually polished for further investigation using the SEM. SEM-EDS shows that the inclusion consists of a Fe-Ni silicide spherule (Figures 2e and 2f; Figures S3 and S4 in Supporting Information S1).

## 2.2. Chicxulub Carbonate-Rich Claystone

Several drilling campaigns have been undertaken within the 200-km-in-diameter (Gulick et al., 2013) and 66.05 Myr old (Sprain et al., 2018) “dino-killer” Chicxulub impact structure in Mexico (Hildebrand et al., 1991), including the IODP-ICDP Expedition 364 during which peak ring samples were recovered (Morgan et al., 2016). The sample investigated in this study is from the IODP-ICDP Expedition 364 drill core, sample 40R1\_36.5–39.0 (recovered between 616.605 and 616.63 m below sea floor; Goderis et al., 2021). The drill core sample is from a transitional unit mainly composed of brown-to-gray carbonate-rich claystone, that is, sediments derived from material transported by tsunami and seiche waves (Goderis et al., 2021). This unit shows elevated Ni, Re, and Os concentrations, and in particular, relatively high Ir concentrations compared to the upper continental crust (Goderis et al., 2021). The sample is approximately 1.0-5.0-5 cm.

### 2.2.1. Results

Both NCT and XCT revealed a banding within the sample (Figures 2g and 2h; bands are oriented east-west in the lower half of the image) corresponding to compositional differences between mainly Al, Si, and Mg, with dark areas (in XCT) being richer in these elements compared to the rest of the sample. Dark bands (low attenuation) in the XCT images are bright in the NCT images and vice versa. The XCT images also revealed numerous highly attenuating spots, which were confirmed by EDS analysis to be iron sulfides (pyrite) grains. Rendering and segmenting of these features show that iron sulfide grains occur mainly in the banded area (Figure 2i). Apart from the banding, other features are possibly obscured by the relatively high hydrogen content of the bulk material as no other features were distinguishable in the NCT images.

## 2.3. Luizi Impact Melt Rock

The 17-km-in-diameter Luizi impact structure is located in the Democratic Republic of the Congo ( $10^{\circ}10'13.5''S/28^{\circ}00'27.0''E$ ) (Ferrière et al., 2011). The investigated sample (LUI13-R1) is a cut fragment of an impact melt rock boulder collected by LF in the year 2013 in a river 6.2 km from the center of the impact structure. The sample contains quartz, alkali feldspar, minor biotite, clinopyroxene, and accessory zircon grains, Fe-Ti oxides, as well as chromite grains, in an aluminosilicate glass (Cavosie et al., 2018; Ferrière et al., 2011). In this study, we scanned a  $\sim 5$ - $5$ - $5$  mm-sized cube of this impact melt rock, aiming to locate potential projectile material and other features of interest.

### 2.3.1. Results

The XCT images revealed two highly attenuating circular features (depicted in purple in Figure 3a) that were not visible in the NCT images. The NCT images are relatively homogenous, except for specks of highly attenuating material that, in one location, form a rounded “blob” around the same location as the circular feature revealed by XCT (Figures 3a and 3b; Figure S5 in Supporting Information S1), which can be clearly seen in a combined rendering of XCT and NCT. Based on the 3D images, the sample was polished down to expose the interior of both the blob and the rim to the surface (Figure 3c) and EDS analysis has confirmed that the rim consists of Fe-oxides and that the blob consists of Mg and Al-rich hydrous clay minerals. Some of the inclusions showing high XCT attenuation (i.e., higher than for the iron oxide grains) correspond to zircon grains (green color in Figure 3a).

## 2.4. Miller Range 03346

The Miller Range (MIL) 03346,231 meteorite belongs to the nakhlite group, which are basaltic meteorites originating from planet Mars (e.g., Bunch & Reid, 1975; Treiman, 2005; Udry et al., 2012). This particular sample



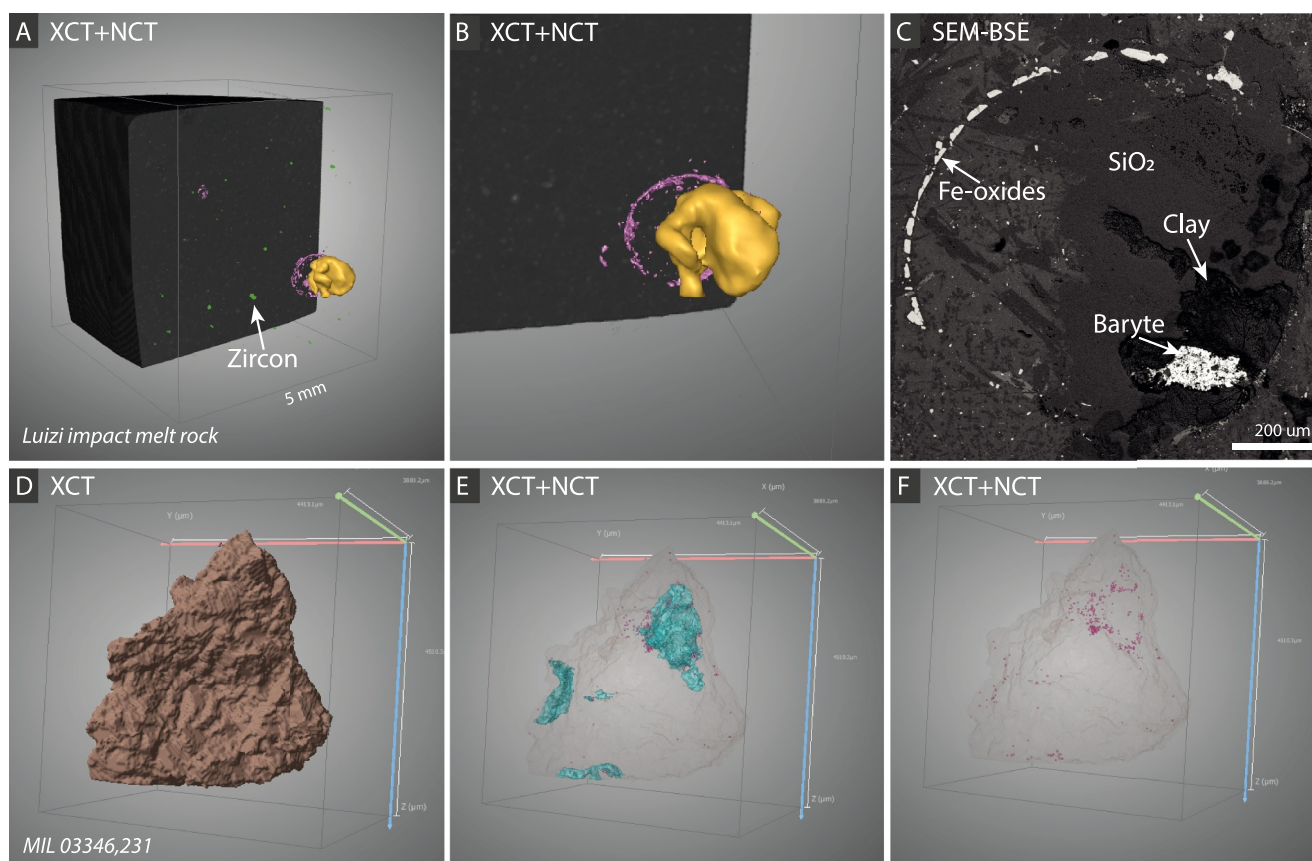


**Figure 3.** (a) XCT volume of Luizi impact melt rock, “clipped” to expose segmented features. The yellow “blob” corresponds to clay (segmented from the neutron computed tomography images). The purple, rounded structure consists of Fe-oxides, and the green inclusions correspond to zircon; both of these are segmented from the XCT images. (b) A close-up showing the clays (yellow), and the association with the Fe-oxide rim (purple). (c) SEM-BSE image showing the Fe-oxide rim, the clay material, and quartz (possibly partly glassy). The bright mineral in the lower right is baryte. (d) Surface rendering of MIL 03346,231. (e) Same as in d, but with the surface rendering set to lower opacity to show the interior. Olivine grains are segmented in turquoise, and hydrous constituents (higher visibility in panel (f)) are in magenta. (f) The hydrous phase (iddingsite) is depicted in magenta. This phase is mainly located within and in the vicinity of the olivine grains.

(MIL 03346,232) is dominated by relatively pristine augite grains and minor olivine crystals, which lie in a fine-grained mesostasis with skeletal titanomagnetite grains. The olivine crystals are cross-cut by iddingsite veins formed by hydrous alteration on Mars (Changela & Bridges, 2010; Lee et al., 2015). The tomography results of this sample were previously reported by Martell et al. (2022).

#### 2.4.1. Results

All major mineral phases within the sample were segmented by thresholding the XCT data. There was a slight overlap in grayscales between augite, mesostasis, and parts of the olivine grains, but generally, the brightest XCT phases corresponded to Fe-Ti oxides and olivine grains. Previous studies have shown that the iddingsite is located mainly within fractures of the olivine grains (Lee et al., 2015), and in some cases in the mesostasis (Daly et al., 2019), which is also where the highest neutron attenuating phase within MIL 03346,231 is found. A 3D rendering with segmented olivine and (hydrous) iddingsite shows that the inferred hydrous material is clustered around the olivine grains (Figures 3d–3f).

### 3. Discussion

We have analyzed a diverse suite of terrestrial impactites and meteorites using a combination of NCT and XCT. With this method, we were able to map the distribution of hydrous alteration in and around olivine grains in nakhlite MIL 03346,231 and in Luizi impact melt rock, and we were also able to find a metal-rich particle in



impact glass. Below, we discuss these results and critically discuss and assess the potential of the methodology used in this study for further investigations.

### 3.1. Impact Events and Traces of the Impactor

Using combined NCT and XCT, we found highly attenuating inclusion in the LDG sample, which was thus a promising candidate for captured projectile material. By polishing the spherule in several steps, the external morphology and the interior of the spherule could be imaged by SEM, and the chemical composition was determined to consist of Fe, Ni, and Si (Figures S2–S4 in Supporting Information S1). To our knowledge, this is the first FeNi silicide (spherule) occurrence in an LDG sample, which either indicates that they are rare and/or were overlooked in previous studies. FeNi silicide inclusions have previously been reported in a sample of the Wabar impact glass (Hamann et al., 2022) but in a significantly smaller size fraction (nanometer-size). They were interpreted to be a mixture of impact-vapor condensates, together with condensates from the ablation of the projectile during its atmospheric entry (Hamann et al., 2022). Metal silicides are also known from several lunar impactite samples (e.g., Gopon et al., 2017; Nazarov et al., 2015) and in meteorites (see discussion and references in Barbaro et al., 2021). The spatial resolution given by NCT would not be sufficient to study nanometer-sized spherules, but the FeNi spherule in our LDG sample shows that using a combination of NCT and XCT can be used to detect inclusions containing projectile material, if large enough. Other impact glasses besides LDG would thus be good targets for combined NCT/XCT, aiming to gain insight into processes taking place during the vaporization of the projectile (and target rocks) and condensation of the spherule.

The Chicxulub core sample was also imaged with NCT and XCT with the aim of locating the projectile material. There is a known iridium anomaly in this core interval (Goderis et al., 2021), but no indications of the presence of PGEs (or other potential projectile material condensates) in the tomographic images were found. The reason could be the very small size (potentially sub-micrometer in size) of the carrier phases of the PGEs, which is below the spatial resolution of our data set, but it could also be due to the heterogenous distribution of PGEs within the interval in which the sample was collected. The high abundance of H in clay minerals (i.e., high neutron attenuation) could possibly also obscure the signal from other elements of interest. This needs to be considered if a sample that is relatively rich in clays, such as the Chicxulub core interval in this study, is chosen for this type of method.

### 3.2. Hydrous Alteration in Meteorites and in Terrestrial Impactites

The sensitivity of NCT to H allows visualization of hydrous phases formed by fluid alteration, while XCT allows to outline the mineral phases and thus to tie hydrous alteration to specific minerals. XCT can also provide a higher spatial resolution than NCT, and thus provide a more detailed view of the sample. Analysis of the tomographic data for MIL 03346,231 shows that iddingsite is mainly concentrated within, or adjacent to, olivine grains, and that there is a limited connection between altered phases, indicating a relatively short duration of the hydrothermal alteration event (Martell et al., 2022). The NCT images of the Luizi impact melt rock sample also revealed regions with hydrated material and a “blob”-like feature (Figures 3a–3c) consisting of clay minerals. In the NCT images, the impact melt rock appears in general relatively homogenous apart from the occurrence of clay minerals. In contrast, most of the highly attenuating phases in the XCT images correspond to zircon (highest attenuation) and Fe-oxide grains, none of which were distinct from the surrounding materials in their neutron attenuation. A bimodal approach that employs both XCT and NCT can thus be used to outline all major mineral phases as well as to interpret the extent of aqueous alteration alongside potential paths of fluid ingress following hydrothermal activity and as a consequence of the degree of weathering of impactite and meteorite samples, which, in turn, provides important clues on the impact cratering process in general and post-impact history recorded by a sample in particular. These investigations can thus shed light on the extent and longevity of hydrothermal systems, with potential consequences for interpretations of habitability.

### 3.3. Method Development

Combined XCT and NCT, is an ideal “first step” in the analysis workflow of heterogenous samples, starting with the least destructive methods to optimize the scientific output as well as ensure representative analysis. Knowledge of the 3D distribution of mineral phases is critical when evaluating and interpreting subsets of a sample via more traditional techniques. For example, fluid pathways, such as fractures penetrating the meteorite

fusion crust, can indicate whether to expect considerable terrestrial contamination within meteorite samples that were not recovered immediately after their fall on Earth. Consequently, by the first imaging the meteorite samples in 3D with NCT and XCT, thin sections can be produced from less weathered regions of the sample. Furthermore, 3D images will provide information about what parts of the sample should be targeted for further detailed studies.

To visualize the tomography images of the different samples, and to enable segmentation and extraction of inclusions, software enabling simultaneous visualization of the 3D images from both modalities slice-by-slice and in a combined 3D rendering mode is important. Phase segmentation can be performed in the dual XCT/NCT images using a bivariate histogram (LaManna et al., 2020; Martell et al., 2022; Treiman et al., 2022), but in samples containing phases with overlapping attenuation values (grayscale), the option to segment manually will enable fine-tuning of the segmentation. In this study, we used the Dragonfly<sup>®</sup> ORS software for data analysis. The workflow for locating inclusions (in this case, the LDG spherule; Figures 2c and 2d) is shown in Figure 4. After aligning the XCT and NCT images and rendering them as one joint image (e.g., in Dragonfly<sup>®</sup> ORS), orthogonal planes can be added to the rendering, and placed so that they intersect directly at the region of interest. In Figure 2b, the planes intersect at the FeNi silicide spherule and using this information, the sample could be cut and polished to expose the spherule at the surface.

### 3.4. Tomography—Truly Non-Destructive?

NCT and XCT are considered to be non-destructive methods, at least at the micro-scale. However, as neutrons and X-rays interact with the sample at an atomic level, both could potentially cause permanent changes to the material properties in certain cases, notably ionization and possibly heating (Hanna & Ketcham, 2017). In dedicated studies on potential changes in samples due to XCT, for example, Ebel et al. (2009) found that synchrotron (a very powerful source of X-rays) tomography did not alter polycyclic aromatic hydrocarbons, while Friedrich et al. (2016), also using synchrotron tomography, found no detectable changes to amino acids. NCT can cause activation of materials by neutron capture, which produces unstable, mainly short-lived, radioactive isotopes. Because of this, samples must be tested for radioactivity before leaving the NCT facility and could be held back depending on the half-lives of the radioactive nuclei. In a recent study, Treiman et al. (2022) reported that their NCT study of a chondrite meteorite sample had a very limited effect (below uncertainty levels in the current analyses) on the isotopic systems of a set of isotopes, for example, Hf-W, within the sample and that NCT caused negligible heating. However, they note that some high-precision isotopic analyses could be affected and that both XCT and NCT will influence thermoluminescence and thus overprint the cosmic ray exposure records within meteorites (see Sears et al., 2016; Treiman et al., 2022). Also, it remains unknown whether NCT has detectable effects on chemical structures (such as might be detectable by e.g., Raman spectroscopy) or on organic molecules of possible relevance in the search for organic markers of extraterrestrial life. Considering that what is undetectable today might be detectable in the future, it is important to take this into account when planning to perform tomography experiments.

### 3.5. Outlook

The spatial resolution is critical when aiming to locate, for example, projectile material, and is as of today a limiting factor in planetary material studies where features of interest are often <10 μm in size or even much smaller in size. Compared to XCT, NCT is still a relatively “niche” technique, but next-generation neutron beamlines could potentially reach sub-μm spatial resolutions. The spatial resolution achievable by NCT depends on several factors, among which is the contrast between the features of interest, the exposure time, and the neutron flux. The interested readers are referred to the practical considerations given in Grosse and Kardjilov (2017). While principally lower flux neutron sources can yield high resolution NCT results, in practice limitations arise concerning highest resolution due to signal-to-noise ratio and long exposure times that are ultimately limited by the available experimental times. Currently, the NeXT imaging beamline instrument at ILL has the highest neutron flux available worldwide ( $\sim 3 \times 10^8$  n/cm<sup>2</sup>/s at the sample position for a collimation ratio of 330) and can provide spatial resolutions below 4 μm, where  $\sim 5$  μm features could be distinguished in tomography that was acquired in  $\sim 11$  hr (Tengattini et al., 2022). In 2013, 13 European countries and more than 100 collaborating institutions partnered up to build the world's most powerful pulsed neutron source, the ESS. ESS will be located in Lund, Sweden, and host 22 state-of-the-art neutron instruments (Andersen et al., 2012). The pulsed neutron source is expected to open to users around the year 2027 and will provide a time average neutron flux comparable to that of the ILL continuous neutron source.

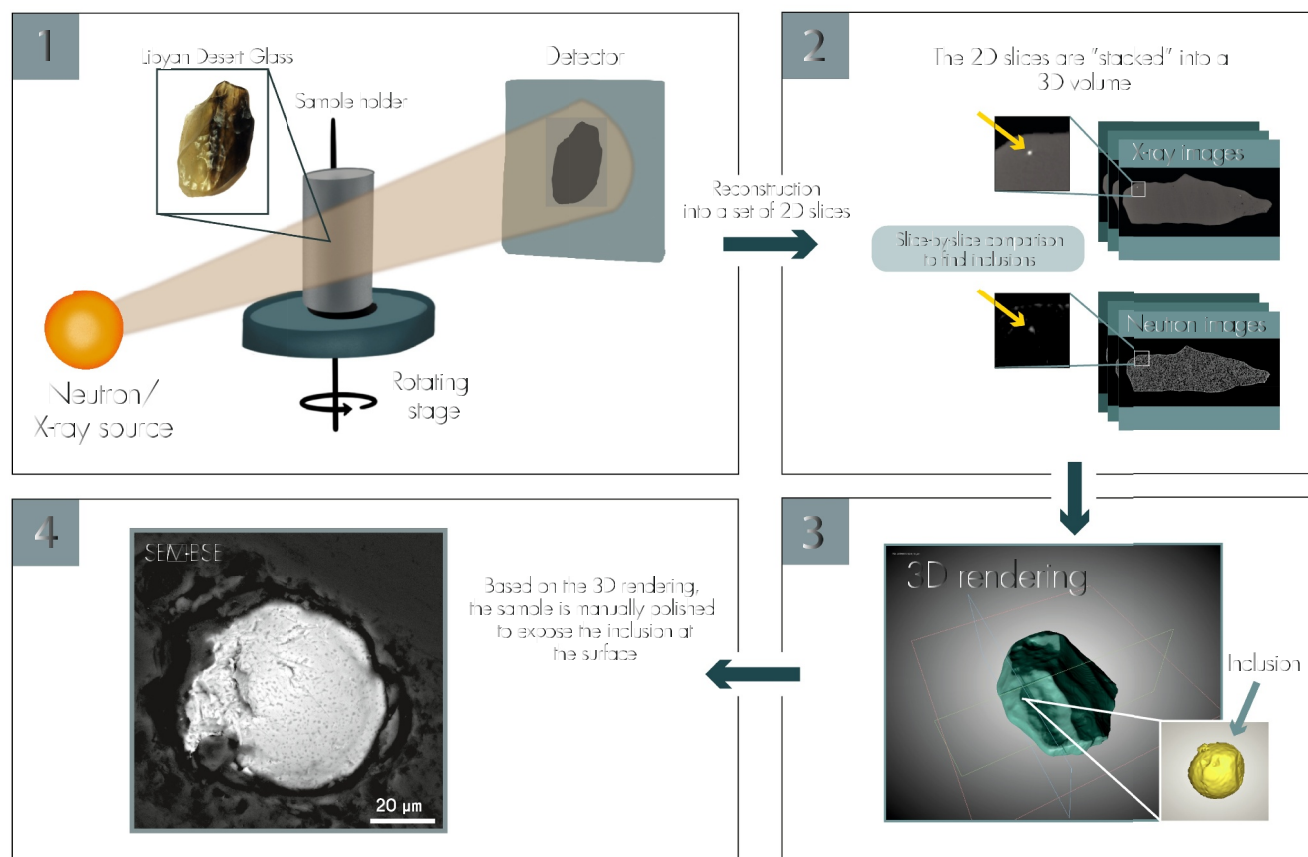


**Figure 4.** Using a combination of neutron computed tomography (NCT) and XCT to locate the projectile material. (1) The sample is placed in a sample holder that is mounted on a rotating stage. A detector measures the decrease in intensity between the incident beam and the final beam after traversing the sample. (2) The tomograms are reconstructed into 2D slices that are then stacked so that they can be viewed as a 3D volume. The two data sets (NCT and XCT) are “registered” (aligned) so that they can be compared slice-by-slice. For the projectile detection, regions-of-interest are inclusions that are highly attenuating for both modalities. (3) If inclusion is found, it can be rendered in 3D and located within the volume. (4) The sample is manually polished to expose the inclusion at the surface.

The samples in these case studies were imaged with a white beam (a broad neutron wavelength spectrum provided by a continuous neutron source). Wavelength-selective neutron imaging can be performed most efficiently at pulsed sources and has the potential for improved quantification and enhanced contrast due to the wavelength dependence of the macroscopic neutron cross section for most elements (Tran et al., 2021). It also enables the exploitation of diffraction contrast that provides the possibility of gaining crystallographic information (Woracek et al., 2018), while inelastic scattering contrast allows to for example, differentiate between different aggregated states of water (Siegwart et al., 2019) and sample temperatures (Al-Falahat et al., 2022), albeit of course these energy-selective methods can increase the exposure time.

Advanced neutron imaging modalities also include phase and dark field contrast (Strobl et al., 2017) as well as polarized imaging (Strobl et al., 2019), which could find applications in planetary science. As mentioned in the previous section, neutron capture gives rise to nuclear processes that enable neutron activation analysis that can be used for elemental analysis and might be combined with tomography (Cazzaniga et al., 2021; Ma et al., 2022). Another powerful application is resonance absorption imaging, where certain isotopes exhibit strong absorption signatures to (high energy) neutrons (Losko & Vogel, 2022; Oba et al., 2023) and could be relevant for planetary geosciences.

Tomography is especially promising for investigating material from sample return missions such as OSIRIS-REx and the NASA/ESA Mars sample return campaign (e.g., Lauretta et al., 2017; Tsuchiyama et al., 2011; Welzenbach et al., 2017) because of the limited amount of material that was and will be returned and in order to maximize the science value of the samples. The Mars Sample Return Planning Group 2 has proposed that XCT should be used for the initial characterization of the Mars 2020 samples before leaving the initial facility and

opening of the sample tubes (Tait et al., 2022). However, more work should be conducted to quantify the effects of both XCT and NCT on the samples, especially on organic compounds, to ensure that the tomography will not compromise later analyses and interpretations (Summons et al., 2014; Tait et al., 2022). Depending on the results of such studies, combined NCT/XCT could be considered early in the preliminary characterization and analysis pipeline to determine sections to target for detailed analyses as well as to provide unique three-dimensional insight into the products of water/rock interactions in the samples.

#### 4. Conclusions

This study highlights that combined NCT and XCT is a powerful non-destructive technique for the study of geologic and planetary materials, especially precious samples such as meteorites and sample-return material. We show that the method can be used to locate and identify projectile material within impactites. We also show that hydrous phases and their spatial distribution can be easily mapped within geologic samples. Combined NCT and XCT can provide guidance for further sample treatment. Non-destructive imaging will be important for several upcoming sample return missions, such as the combined NASA/ESA Mars sample return campaign, and combined NCT and XCT will provide unique insights into the material without a little or no sample preparation.

#### Data Availability Statement

For NCT and XCT data, see Martell (2022, 2023).

#### References

- About, T. (2009). Libyan Desert Glass: Has the enigma of its origin been resolved? *Physics Procedia*, 2(3), 1425–1432. <https://doi.org/10.1016/j.phpro.2009.11.112>
- Al-Falahat, A. M., Kardjilov, N., Woracek, R., Boin, M., Markotter, H., Kuhn, L. T., et al. (2022). Temperature dependence in Bragg edge neutron transmission measurements. *Journal of Applied Crystallography*, 55(4), 919–928. <https://doi.org/10.1107/S1600576722006549>
- Alvarez, L. W., Alvarez, W., Asaro, F., & Michel, H. V. (1980). Extraterrestrial cause for the Cretaceous-Tertiary extinction. *Science*, 208(4448), 1095–1108. <https://doi.org/10.1126/science.208.4448.1095>
- Alwmark, C., Schmitz, B., Holm, S., Marone, F., & Stampanoni, M. (2011). A 3-D study of mineral inclusions in chromite from ordinary chondrites using synchrotron radiation X-ray tomographic microscopy—Method and applications. *Meteoritics & Planetary Sciences*, 46(8), 1071–1081. <https://doi.org/10.1111/j.1945-5100.2011.01214.x>
- Andersen, K. H., Argyriou, D. N., Batkov, C., Böhme, S., Bousson, I., Bustinduy, C., et al. (2012). ESS conceptual design report (CDR, 2012). E. S. Source. <https://europespallationsource.se/publications>
- Andersen, K. H., Argyriou, D. N., Jackson, A. J., Houston, J., Henry, P. F., Deen, P. P., et al. (2020). The instrument suite of the European Spallation Source. *Nuclear Instruments and Methods in Physics Research Section A: Accelerators, Spectrometers, Detectors and Associated Equipment*, 957, 163402. <https://doi.org/10.1016/j.nima.2020.163402>
- Barbaro, A., Domeneghetti, M. C., Litasov, K. D., Ferrière, L., Pittarello, L., Christ, O., et al. (2021). Origin of micrometer-sized impact diamonds in ureilites by catalytic growth involving Fe-Ni-silicide: The example of Kenna meteorite. *Geochimica et Cosmochimica Acta*, 309, 286–298. <https://doi.org/10.1016/j.gca.2021.06.022>
- Beatty, D. W., Grady, M. M., McSween, H. Y., Sefton-Nash, E., Carrier, L., Altieri, F., et al. (2019). The potential science and engineering value of samples delivered to Earth by Mars sample return. *Meteoritics & Planetary Sciences*, 54(S1), S3–S152. <https://doi.org/10.1111/maps.13242>
- Bigazzi, G., & De Michele, V. (1996). New fission-track age determinations on impact glasses. *Meteoritics & Planetary Sciences*, 31(2), 234–236. <https://doi.org/10.1111/j.1945-5100.1996.tb02017.x>
- Brownlee, D., Tsou, P., Aléon, J., Alexander, C. M. O. D., Araki, T., Bajt, S., et al. (2006). Comet 81P/wild 2 under a microscope. *Science*, 314(5806), 1711–1716. <https://doi.org/10.1126/science.1135840>
- Bunch, T. E., & Reid, A. M. (1975). The nakhlites Part I: Petrography and mineral chemistry. *Meteoritics*, 10(4), 303–315. <https://doi.org/10.1111/j.1945-5100.1975.tb01187.x>
- Caporali, S., Grazi, F., Salvemini, F., Garbe, U., Peetermans, S., & Pratesi, G. (2016). Structural Characterization of iron meteorites through neutron tomography. *Minerals*, 6(1), 14. <https://doi.org/10.3390/min6010014>
- Cavosie, A. J., & Koeberl, C. (2019). Overestimation of threat from 100 Mt-class airbursts? High-Pressure evidence from zircon in Libyan Desert Glass. *Geology*, 47(7), 609–612. <https://doi.org/10.1130/G45974.1>
- Cavosie, A. J., Timms, N. E., Ferrière, L., & Rochette, P. (2018). FRIGN zircon—The only terrestrial mineral diagnostic of high-pressure and high-temperature shock deformation. *Geology*, 46(10), 891–894. <https://doi.org/10.1130/G45079.1>
- Cazzaniga, C., Scherillo, A., Fedrigo, A., Raspino, D., Grazi, F., & Frost, C. D. (2021). Neutron activation analysis of archeological artifacts using the ISIS pulsed neutron source. *AIP Advances*, 11(7), 075005. <https://doi.org/10.1063/5.0043935>
- Changela, H. G., & Bridges, J. C. (2010). Alteration assemblages in the nakhlites: Variation with depth on Mars. *Meteoritics & Planetary Sciences*, 45(12), 1847–1867. <https://doi.org/10.1111/j.1945-5100.2010.01123.x>
- Che, X., Nemchin, A., Liu, D., Long, T., Wang, C., Norman, M. D., et al. (2021). Age and composition of young basalts on the Moon, measured from samples returned by Chang'e-5. *Science*, 374(6569), 887–890. <https://doi.org/10.1126/science.abc17957>
- Cipriani, C., Corazza, M., Giuli, G., Moggi Cecchi, V., Pratesi, G., Rossi, P., & Vittone, E. (2000). Ion beam study of a possible extraterrestrial body signature in Libyan desert glass. *Nuclear Instruments and Methods in Physics Research Section B: Beam Interactions with Materials and Atoms*, 170(1), 187–192. [https://doi.org/10.1016/S0168-583X\(00\)00113-0](https://doi.org/10.1016/S0168-583X(00)00113-0)
- Cnudde, V., & Boone, M. N. (2013). High-resolution X-ray computed tomography in geosciences: A review of the current technology and applications. *Earth-Science Reviews*, 123, 1–17. <https://doi.org/10.1016/j.earscirev.2013.04.003>



- Daly, L., Lee, M. R., Piazzolo, S., Griffin, S., Bazargan, M., Campanale, F., et al. (2019). Boom boom pow: Shock-facilitated aqueous alteration and evidence for two shock events in the Martian nakhlite meteorites. *Science Advances*, 5(9), eaaw5549. <https://doi.org/10.1126/sciadv.aaw5549>
- Day, J. M. D., Taylor, L. A., Floss, C., & McSween, H. Y. (2006). Petrology and chemistry of MIL 03346 and its significance in understanding the petrogenesis of nakhlites on Mars. *Meteoritics & Planetary Sciences*, 41(4), 581–606. <https://doi.org/10.1111/j.1945-5100.2006.tb00484.x>
- Dragonfly 2021.1. (2021). Dragonfly 2021.1 [Computer software]. Object Research Systems (ORS) Inc. <http://www.theobjects.com/dragonfly>
- Ebel, D. S., Greenberg, M., Rivers, M. L., & Newville, M. (2009). Three-dimensional textural and compositional analysis of particle tracks and fragmentation history in aerogel. *Meteoritics & Planetary Sciences*, 44(10), 1445–1463. <https://doi.org/10.1111/j.1945-5100.2009.tb01185.x>
- Faragó, T., Gasilov, S., Emslie, I., Zuber, M., Helfen, L., Vogelgesang, M., & Baumbach, T. (2022). Tofu: A fast, versatile and user-friendly image processing toolkit for computed tomography. *Journal of Synchrotron Radiation*, 29(3), 916–927. <https://doi.org/10.1107/S160057752200282X>
- Farley, K. A., Stack, K. M., Shuster, D. L., Horgan, B. H. N., Hurowitz, J. A., Tarnas, J. D., et al. (2022). Aqueously altered igneous rocks sampled on the floor of Jezero crater, Mars. *Science*, 377(6614), eabo2196. <https://doi.org/10.1126/science.abo2196>
- Farmer, J. (2000). Hydrothermal systems: Doorways to early biosphere evolution. *Geological Society of America Today*, 10(7), 1–9.
- Fedrigo, A., Marstal, K., Bender Koch, C., Andersen Dahl, V., BJORHOLM DAHL, A., Lyksborg, M., et al. (2018). Investigation of a Monturaqui impactite by means of bi-modal X-ray and neutron tomography. *Journal of Imaging*, 4(5), 72. <https://doi.org/10.3390/jimaging4050072>
- Feignon, J.-G., Schulz, T., Ferrière, L., Goderis, S., de Graaff, S. J., Kaskes, P., et al. (2022). Search for a meteoritic component within the impact melt rocks of the Chicxulub impact structure peak ring, Mexico. *Geochimica et Cosmochimica Acta*, 323, 74–101. <https://doi.org/10.1016/j.gca.2022.02.006>
- Ferrière, L., Lubala, F. R. T., Osinski, G. R., & Kaseti, P. K. (2011). The newly confirmed Luizi impact structure, Democratic Republic of Congo —Insights into central uplift formation and post-impact erosion. *Geology*, 39(9), 851–854. <https://doi.org/10.1130/G31990.1>
- French, B. M. (1998). *Traces of catastrophe: A handbook of shock-metamorphic effects in terrestrial meteorite impact structures* (Vol. 954). Lunar and Planetary Institute.
- Friedrich, J. M., Glavin, D. P., Rivers, M. L., & Dworkin, J. P. (2016). Effect of a synchrotron X-ray microtomography imaging experiment on the amino acid content of a CM chondrite. *Meteoritics & Planetary Sciences*, 51(2), 429–437. <https://doi.org/10.1111/maps.12595>
- Giuli, G., Paris, E., Pratesi, G., Koeberl, C., & Cipriani, C. (2003). Iron oxidation state in the Fe-rich layer and silica matrix of Libyan Desert Glass: A high-resolution XANES study. *Meteoritics & Planetary Sciences*, 38(8), 1181–1186. <https://doi.org/10.1111/j.1945-5100.2003.tb00306.x>
- Goderis, S., Paquay, F., & Claeys, P. (2012). Projectile identification in terrestrial impact structures and ejecta material. In G. R. Osinski & E. Pierazzo (Eds.), *Impact cratering: Processes and products* (pp. 223–239). Blackwell Publishing Ltd. <https://doi.org/10.1002/9781118447307.ch15>
- Goderis, S., Sato, H., Ferrière, L., Schmitz, B., Burney, D., Kaskes, P., et al. (2021). Globally distributed iridium layer preserved within the Chicxulub impact structure. *Science Advances*, 7(9), eabe3647. <https://doi.org/10.1126/sciadv.abe3647>
- Goderis, S., Simonson, B. M., McDonald, I., Hassler, S. W., Izmer, A., Belza, J., et al. (2013). Ni-rich spinels and platinum group element nuggets condensed from a Late Archaean impact vapour cloud. *Earth and Planetary Science Letters*, 376, 87–98. <https://doi.org/10.1016/j.epsl.2013.06.027>
- Gopon, P., Spicuzza, M. J., Kelly, T. F., Reinhard, D., Prosa, T. J., & Fournelle, J. (2017). Ultra-reduced phases in Apollo 16 regolith: Combined field emission electron probe microanalysis and atom probe tomography of submicron Fe-Si grains in Apollo 16 sample 61500. *Meteoritics & Planetary Sciences*, 52(9), 1941–1962. <https://doi.org/10.1111/maps.12899>
- Gross, J., Mosie, A. B., Zeigler, R. A., McCubbin, F. M., & Shearer, C. K., & ANGSA science team. (2023). Preparing for artemis with ANGSA: The dissection and characterization of previously unopened and sealed double drive tube 73001/2. *Microscopy and Microanalysis*, 29(Supplement\_1), 838–839. <https://doi.org/10.1093/micmic/ozad067.416>
- Grosse, M., & Kardjilov, N. (2017). Which resolution can be achieved in practice in neutron imaging experiments? – A general view and application on the Zr-ZrH<sub>2</sub> and ZrO<sub>2</sub>-ZrN systems. *Physics Procedia*, 88, 266–274. <https://doi.org/10.1016/j.phpro.2017.06.037>
- Gulick, S. P. S., Christeson, G. L., Barton, P. J., Grieve, R. A. F., Morgan, J. V., & Urrutia-Fucugauchi, J. (2013). Geophysical characterization of the Chicxulub impact crater. *Reviews of Geophysics*, 51(1), 31–52. <https://doi.org/10.1002/rog.20007>
- Hamann, C., Artemieva, N., Wirth, R., Roddatis, V., & Kearsley, A. (2022). *Condensation of iron-nickel silicides and silicon monoxide from impact vapor plumes: A case study on the Wabar impact glasses*. 85th Annual Meeting of The Meteoritical Society.
- Hanna, R. D., & Ketcham, R. A. (2017). X-ray computed tomography of planetary materials: A primer and review of recent studies. *Geochemistry*, 77(4), 547–572. <https://doi.org/10.1016/j.chemer.2017.01.006>
- Hanna, R. D., Ketcham, R. A., Edey, D. R., & O'Connell, J. (2022). 3D porosity structure of the earliest solar system material. *Scientific Reports*, 12(1), 8369. <https://doi.org/10.1038/s41598-022-11976-1>
- Hezel, D. C., Elangovan, P., Viehmann, S., Howard, L., Abel, R. L., & Armstrong, R. (2013). Visualisation and quantification of CV chondrite petrography using micro-tomography. *Geochimica et Cosmochimica Acta*, 116, 33–40. <https://doi.org/10.1016/j.gca.2012.03.015>
- Hezel, D. C., Friedrich, J. M., & Uesugi, M. (2013). Looking inside: 3D structures of meteorites. *Geochimica et Cosmochimica Acta*, 116, 1–4. <https://doi.org/10.1016/j.gca.2013.01.012>
- Hildebrand, A. R., Penfield, G. T., Kring, D. A., Pilkington, M., Camargo, Z. A., Jacobsen, S. B., & Boynton, W. V. (1991). Chicxulub Crater: A possible Cretaceous/Tertiary boundary impact crater on the Yucatán Peninsula, Mexico. *Geology*, 19(9), 867–871. [https://doi.org/10.1130/0091-7613\(1991\)019<0867:CCAPCT>2.3.CO;2](https://doi.org/10.1130/0091-7613(1991)019<0867:CCAPCT>2.3.CO;2)
- Kadlag, Y., Haberthür, D., Leya, I., Hlushchuk, R., & Mezger, K. (2023). Physical properties and average atomic numbers of chondrules using computed tomography. *Planetary and Space Science*, 238, 105799. <https://doi.org/10.1016/j.pss.2023.105799>
- Kaestner, A. P., Hartmann, S., Kühne, G., Frei, G., Grünzweig, C., Josic, L., et al. (2011). The ICON beamline – A facility for cold neutron imaging at SINQ. *Nuclear Instruments and Methods in Physics Research Section A: Accelerators, Spectrometers, Detectors and Associated Equipment*, 659(1), 387–393. <https://doi.org/10.1016/j.nima.2011.08.022>
- Kardjilov, N., Manke, I., Woracek, R., Hilger, A., & Banhart, J. (2018). Advances in neutron imaging. *Materials Today*, 21(6), 652–672. <https://doi.org/10.1016/j.mattod.2018.03.001>
- Kawaguchi, J. I., Fujiwara, A., & Uesugi, T. (2008). Hayabusa—Its technology and science accomplishment summary and Hayabusa-2. *Acta Astronautica*, 62(10), 639–647. <https://doi.org/10.1016/j.actaastro.2008.01.028>
- Kichanov, S. E., Abdurakhimov, B. A., Zel, I. Y., Kirillov, A. K., Kozlenko, D. P., Lapina, I. K., & Mentsin, Y. L. (2022). The structural analysis of Kunya-Urgench chondrite: The nondestructive neutron studies. *Meteoritics & Planetary Sciences*, 57(10), 1836–1845. <https://doi.org/10.1111/maps.13903>
- Koeberl, C. (1998). Identification of meteoritic components in impactites. *Geological Society, London, Special Publications*, 140(1), 133–153. <https://doi.org/10.1144/GSL.SP.1998.140.01.11>

- Koeberl, C. (2000). Confirmation of a meteoritic component in Libyan Desert Glass from osmium-isotopic data. *Meteoritics & Planetary Sciences*, 35, A89–A90. <http://adsabs.harvard.edu/abs/2000M%26PSA...35Q..89K>
- Koeberl, C., Claey's, P., Hecht, L., & McDonald, I. (2012). Geochemistry of impactites. *Elements*, 8(1), 37–42. <https://doi.org/10.2113/gselements.8.1.37>
- Koeberl, C., Denison, C., Ketcham, R., & Reimold, W. (2002). High-resolution X-ray computed tomography of impactites. *Journal of Geophysical Research*, 107(E10), 5089. <https://doi.org/10.1029/2001JE001833>
- Koeberl, C., & Shirey, S. B. (1997). Re–Os isotope systematics as a diagnostic tool for the study of impact craters and distal ejecta. *Palaeogeography, Palaeoclimatology, Palaeoecology*, 132(1), 25–46. [https://doi.org/10.1016/S0031-0182\(97\)00045-X](https://doi.org/10.1016/S0031-0182(97)00045-X)
- Koeberl, C., Shukolyukov, A., & Lugmair, G. W. (2007). Chromium isotopic studies of terrestrial impact craters: Identification of meteoritic components at Bosumtwi, Clearwater East, Lappajärvi, and Rochechouart. *Earth and Planetary Science Letters*, 256(3), 534–546. <https://doi.org/10.1016/j.epsl.2007.02.008>
- Kring, D. A., Tikoo, S. M., Schmieder, M., Riller, U., Rebolledo-Vieyra, M., Simpson, S. L., et al. (2020). Probing the hydrothermal system of the Chicxulub impact crater. *Science Advances*, 6(22), eaaz3053. <https://doi.org/10.1126/sciadv.aaz3053>
- Krzysińska, A. (2011). High resolution X-ray tomography as a tool for analysis of internal textures in meteorites. *Meteorites*, 01, 3–12. <https://doi.org/10.5277/met110101>
- LaManna, J. M., Chen, J.-H., Althaus, S., Liu, Y., Hussey, D., & Jacobson, D. (2020). Bivariate histogram segmentation of simultaneous neutron and X-ray tomography for improved compositional and structural determination of source rock shales. *Microscopy and Microanalysis*, 26(Suppl. 2), 3220–3221. <https://doi.org/10.1017/S1431927620024204>
- LaManna, J. M., Hussey, D. S., Baltic, E., & Jacobson, D. L. (2017). Neutron and X-ray Tomography (NeXT) system for simultaneous, dual modality tomography. *Review of Scientific Instruments*, 88(11), 113702. <https://doi.org/10.1063/1.4989642>
- Lauretta, D. S., Balram-Knutson, S. S., Beshore, E., Boynton, W. V., Drouot d'Aubigny, C., DellaGiustina, D. N., et al. (2017). OSIRIS-REx: Sample return from asteroid (101955) Bennu. *Space Science Reviews*, 212(1), 925–984. <https://doi.org/10.1007/s11214-017-0405-1>
- Lee, M. R., Tomkinson, T., Hallis, L. J., & Mark, D. F. (2015). Formation of iddingsite veins in the martian crust by centripetal replacement of olivine: Evidence from the nakhlite meteorite Lafayette. *Geochimica et Cosmochimica Acta*, 154, 49–65. <https://doi.org/10.1016/j.gca.2015.01.022>
- Lehmann, E., & Kardjilov, N. (2008). Neutron absorption tomography. In J. Banhart (Ed.), *Advanced tomographic methods in materials research and engineering*. Oxford University Press. <https://doi.org/10.1093/acprof:oso/9780199213245.001.0001>
- Lehmann, E., Mannes, D., Henss, M., & Speidel, M. (2022). Ancient buddhist metal statues using neutron tomography. In S. D'Amico & V. Venuti (Eds.), *Handbook of cultural heritage analysis*. Springer. [https://doi.org/10.1007/978-3-030-60016-7\\_11](https://doi.org/10.1007/978-3-030-60016-7_11)
- Lemelle, L., Simionovici, A., Truche, R., Rau, C., Chukalina, M., & Gillet, P. (2004). A new nondestructive X-ray method for the determination of the 3D mineralogy at the micrometer scale. *American Mineralogist*, 89(4), 547–553. <https://doi.org/10.2138/am-2004-0409>
- Liu, Y., Tice, M. M., Schmidt, M. E., Treiman, A. H., Kizovski, T. V., Hurowitz, J. A., et al. (2022). An olivine cumulate outcrop on the floor of Jezero crater, Mars. *Science*, 377(6614), 1513–1519. <https://doi.org/10.1126/science.abo2756>
- Lock, S. J., Bermingham, K. R., Parai, R., & Boyet, R. (2020). Geochemical constraints on the origin of the Moon and preservation of ancient terrestrial heterogeneities. *Space Science Reviews*, 216(6), 109. <https://doi.org/10.1007/s11214-020-00729-z>
- Losko, A. S., & Vogel, S. C. (2022). 3D isotope density measurements by energy-resolved neutron imaging. *Scientific Reports*, 12(1), 6648. <https://doi.org/10.1038/s41598-022-10085-3>
- Ma, Y., Yang, X., Huo, H., Li, H., Wang, S., Huang, H., & Chen, H. (2022). Measurement study of neutron field relative distribution in sample for PGNA based on NT. *Nuclear Instruments and Methods in Physics Research Section A: Accelerators, Spectrometers, Detectors and Associated Equipment*, 1045, 167451. <https://doi.org/10.1016/j.nima.2022.167451>
- Martell, J. (2022). The scale of a Martian hydrothermal system explored using combined neutron and X-ray tomography [Dataset]. Zenodo. <https://doi.org/10.5281/zenodo.6365242>
- Martell, J. (2023). [Dataset]. Zenodo. <https://doi.org/10.5281/zenodo.8384086>
- Martell, J., Alwmark, C., Daly, L., Hall, S., Alwmark, S., Woracek, R., et al. (2022). The scale of a martian hydrothermal system explored using combined neutron and x-ray tomography. *Science Advances*, 8(19), eabn3044. <https://doi.org/10.1126/sciadv.abn3044>
- Mohr-Westheide, T., Greshake, A., Wirth, R., & Reimold, W. U. (2018). Transmission electron microscopy of impact-generated platinum group element alloys from Barberton spherule layers: New clues to their formation. *Meteoritics & Planetary Sciences*, 53(7), 1516–1536. <https://doi.org/10.1111/maps.13109>
- Morgan, J. V., Gulick, S. P., Bralower, T., Chenot, E., Christeson, G., Claey's, P., et al. (2016). The formation of peak rings in large impact craters. *Science*, 354(6314), 878–882. <https://doi.org/10.1126/science.aah6561>
- Murchie, S., Arvidson, R., Bedini, P., Beisser, K., Bibring, J. P., Bishop, J., et al. (2007). Compact reconnaissance imaging spectrometer for Mars (CRISM) on Mars reconnaissance orbiter (MRO). *Journal of Geophysical Research*, 112(E05S03). <https://doi.org/10.1029/2006JE002682>
- Nazarov, M. A., Shornikov, S. I., & Demidova, S. I. (2015). Origin of native silicon and iron silicides in the Dhofar 280 lunar meteorite. *Petrology*, 23(2), 168–175. <https://doi.org/10.1134/S0869591115020071>
- Needham, A. W., Bilheux, H. Z., Eckley, S. A., & Zeigler, R. A. (2020). Coordinated analyses of chondrites using neutron and X-ray computed tomography, and electron microscopy, 51st lunar and planetary science conference.
- Oba, Y., Motokawa, R., Kaneko, K., Nagai, T., Tsuchikawa, Y., Shinohara, T., et al. (2023). Neutron resonance absorption imaging of simulated high-level radioactive waste in borosilicate glass. *Scientific Reports*, 13(1), 10071. <https://doi.org/10.1038/s41598-023-37157-2>
- Osinski, G. R., Grieve, R. A. F., Ferrière, L., Losiak, A., Pickersgill, A., Cavosie, A. J., et al. (2022). Impact Earth: A review of the terrestrial impact record. *Earth-Science Reviews*, 232, 104112. <https://doi.org/10.1016/j.earscirev.2022.104112>
- Osinski, G. R., Tornabene, L. L., Banerjee, N. R., Cockell, C. S., Flemming, R., Izawa, M. R. M., et al. (2013). Impact-generated hydrothermal systems on Earth and Mars. *Icarus*, 224(2), 347–363. <https://doi.org/10.1016/j.icarus.2012.08.030>
- Pakhnevich, A. (2016). *On the application of tomography techniques to search for water and organic matter in meteorites*. Bruker microCT User Meeting.
- Peetermans, S., Grazi, F., Salvemini, F., Lehmann, E. H., Caporali, S., & Pratesi, G. (2013). Energy-selective neutron imaging for morphological and phase analysis of iron-nickel meteorites. *Analyst*, 138(18), 5303–5308. <https://doi.org/10.1039/C3AN00985H>
- Schindelin, J., Arganda-Carreras, I., Frise, E., Kaynig, V., Longair, M., Pietzsch, T., et al. (2012). Fiji: An open-source platform for biological-image analysis. *Nature Methods*, 9(7), 676–682. <https://doi.org/10.1038/nmeth.2019>
- Schulte, P., Alegret, L., Arenillas, I., Arz, J. A., Barton, P. J., Bown, P. R., et al. (2010). The Chicxulub asteroid impact and Mass extinction at the Cretaceous-Paleogene Boundary. *Science*, 327(5970), 1214–1218. <https://doi.org/10.1126/science.1177265>
- Sears, D. W. G., Sears, H., Ebel, D. S., Wallace, S., & Friedrich, J. M. (2016). X-ray computed tomography imaging: A not-so-nondestructive technique. *Meteoritics & Planetary Sciences*, 51(4), 833–838. <https://doi.org/10.1111/maps.12622>

- Sears, V. F. (1992). Neutron scattering lengths and cross sections. *Neutron News*, 3(3), 26–37. <https://doi.org/10.1080/10448639208218770>
- Siegiwart, M., Woracek, R., Márquez Damián, J. I., Tremsin, A. S., Manzi-Orezzoli, V., Strobl, M., et al. (2019). Distinction between super-cooled water and ice with high duty cycle time-of-flight neutron imaging. *Review of Scientific Instruments*, 90(10), 103705. <https://doi.org/10.1063/1.5110288>
- Soini, A.-J., Kukkonen, I. T., Suhonen, H., Lukić, B., Kohout, T., & Luttinen, A. V. (2023). Investigation of the porosity of L/LL4 ordinary chondrite Bjurböle using synchrotron radiation microtomography and scanning electron microscopy: Implications for parent body evolution. *Physics of the Earth and Planetary Interiors*, 343, 107087. <https://doi.org/10.1016/j.pepi.2023.107087>
- Sprain, C. J., Renne, P. R., Clemens, W. A., & Wilson, G. P. (2018). Calibration of chron C29r: New high-precision geochronologic and paleomagnetic constraints from the Hell Creek region, Montana. *GSA Bulletin*, 130(9–10), 1615–1644. <https://doi.org/10.1130/B31890.1>
- Stamati, O., Andò, E., Roubin, E., Cailletaud, R., Wiebicke, M., Pinzon, G., et al. (2020). SPAM: Software for practical analysis of materials. *Journal of Open Source Software*, 5(51), 2286. <https://doi.org/10.21105/joss.02286>
- Steen Duchnik, S., Lanzky, M., & Steffensen Schmidt, L. (2012). *X-ray and neutron tomography of the Allende meteorite* (Bachelor Thesis). Copenhagen University. Retrieved from <https://nbi.ku.dk/english/theses/bachelor-theses/sandra-duchnik-mika-lanzky-and-louise-schmidt/>
- Strobl, M., Harti, R. P., Gruenzweig, C., Woracek, R., & Plomp, J. (2017). Small angle scattering in neutron imaging—A review. *Journal of Imaging*, 3(4), 64. <https://doi.org/10.3390/jimaging3040064>
- Strobl, M., Heimonen, H., Schmidt, S., Sales, M., Kardjilov, N., Hilger, A., et al. (2019). Polarization measurements in neutron imaging. *Journal of Physics D: Applied Physics*, 52(12), 123001. <https://doi.org/10.1088/1361-6463/aafa5e>
- Strobl, M., Manke, I., Kardjilov, N., Hilger, A., Dawson, M., & Banhart, J. (2009). Advances in neutron radiography and tomography. *Journal of Physics D: Applied Physics*, 42(24), 243001. <https://doi.org/10.1088/0022-3727/42/24/243001>
- Summons, R. E., Sessions, A. L., Allwood, A. C., Barton, H. A., Beaty, D. W., Blakkolb, B., et al. (2014). Planning considerations related to the organic contamination of Martian samples and implications for the Mars 2020 Rover. *Astrobiology*, 14(12), 969–1027. <https://doi.org/10.1089/ast.2014.1244>
- Tagle, R., & Claeys, P. (2005). An ordinary chondrite impactor for the Popigai crater, Siberia. *Geochimica et Cosmochimica Acta*, 69(11), 2877–2889. <https://doi.org/10.1016/j.gca.2004.11.024>
- Tait, K. T., McCubbin, F. M., Smith, C. L., Agee, C. B., Busemann, H., Cavalazzi, B., et al. (2022). Preliminary planning for Mars Sample Return (MSR) Curation activities in a sample receiving facility (SRF). *Astrobiology*, 22(S1), S–57–S–80. <https://doi.org/10.1089/ast.2021.0105>
- Tengattini, A., Kardjilov, N., Helfen, L., Douissard, P.-A., Lenoir, N., Markötter, H., et al. (2022). Compact and versatile neutron imaging detector with sub-4µm spatial resolution based on a single-crystal thin-film scintillator. *Optics Express*, 30(9), 14461–14477. <https://doi.org/10.1364/OE.448932>
- Tengattini, A., Lenoir, N., Andò, E., Giroud, B., Atkins, D., Beaucour, J., & Viggiani, G. (2020). NeXT-grenoble, the neutron and X-ray tomograph in Grenoble. *Nuclear Instruments and Methods in Physics Research Section A: Accelerators, Spectrometers, Detectors and Associated Equipment*, 968, 163939. <https://doi.org/10.1016/j.nima.2020.163939>
- Tengattini, A., Lenoir, N., Andò, E., & Viggiani, G. (2021). Neutron imaging for geomechanics: A review. *Geomechanics for Energy and the Environment*, 27, 100206. <https://doi.org/10.1016/j.gete.2020.100206>
- Toulmin, P., Baird, A. K., Clark, B. C., Keil, K., Rose, H. J., Jr., Christian, R. P., et al. (1977). Geochemical and mineralogical interpretation of the Viking inorganic chemical results. *Journal of Geophysical Research*, 82(28), 4625–4634. <https://doi.org/10.1029/JS082i028p04625>
- Tran, K. V., Woracek, R., Kardjilov, N., Markötter, H., Hilger, A., Kockelmann, W., et al. (2021). Spectral neutron tomography. *Materials Today Advances*, 9, 100132. <https://doi.org/10.1016/j.mtadv.2021.100132>
- Treiman, A., LaManna, J., Hussey, D., deClue, I., & Anovitz, L. (2022). Coordinated neutron and X-ray computed tomography of meteorites: Detection and distribution of hydrogen-bearing materials. *Meteoritics & Planetary Sciences*, 57(10), 1820–1835. <https://doi.org/10.1111/maps.13904>
- Treiman, A. H. (2005). The nakhlite meteorites: Augite-rich igneous rocks from Mars. *Geochemistry*, 65(3), 203–270. <https://doi.org/10.1016/j.chemer.2005.01.004>
- Treiman, A. H., LaManna, J. M., Anovitz, L. M., Hussey, D. S., & Jacobson, D. L. (2018). Neutron computed tomography of meteorites: Detecting hydrogen-bearing materials. 49th lunar and planetary science conference.
- Tschiyama, A., Nakano, T., Uesugi, K., Uesugi, M., Takeuchi, A., Suzuki, Y., et al. (2013). Analytical dual-energy microtomography: A new method for obtaining three-dimensional mineral phase images and its application to Hayabusa samples. *Geochimica et Cosmochimica Acta*, 116, 5–16. <https://doi.org/10.1016/j.gca.2012.11.036>
- Tschiyama, A., Uesugi, M., Matsushima, T., Michikami, T., Kadono, T., Nakamura, T., et al. (2011). Three-dimensional structure of Hayabusa samples: Origin and evolution of Itokawa regolith. *Science*, 333(6046), 1125–1128. <https://doi.org/10.1126/science.1207807>
- Udry, A., Mc Sween, J. H. Y., Lecumberri-Sanchez, P., & Bodnar, R. J. (2012). Paired nakhlites MIL 090030, 090032, 090136, and 03346: Insights into the Miller Range parent meteorite. *Meteoritics & Planetary Sciences*, 47(10), 1575–1589. <https://doi.org/10.1111/j.1945-5100.2012.01420.x>
- Welzenbach, L. C., Fries, M. D., Grady, M. M., Greenwood, R. C., McCubbin, F. M., Zeigler, R. A., et al. (2017). X-ray computed tomography: The first step in Mars sample return processing, 48th lunar and planetary science conference.
- Woracek, R., Santisteban, J., Fedrigo, A., & Strobl, M. (2018). Diffraction in neutron imaging—A review. *Nuclear Instruments and Methods in Physics Research Section A: Accelerators, Spectrometers, Detectors and Associated Equipment*, 878, 141–158. <https://doi.org/10.1016/j.nima.2017.07.040>
- Yada, T., Abe, M., Okada, T., Nakato, A., Yagata, K., Miyazaki, A., et al. (2022). Preliminary analysis of the Hayabusa2 samples returned from C-type asteroid Ryugu. *Nature Astronomy*, 6(2), 214–220. <https://doi.org/10.1038/s41550-021-01550-6>
- Zubov, A. A., Shumilova, T. G., Zhuravlev, A. V., & Isaenko, S. I. (2021). X-ray computed microtomography of diamondiferous impact suevitic breccia and clast-poor melt rock from the Kara astrobleme (Pay-Khoy, Russia). *American Mineralogist*, 106(11), 1860–1870. <https://doi.org/10.2138/am-2021-7578>